INTERNATIONAL JOURNAL FOR NUMERICAL METHODS IN FLUIDS, VOL. 24, 615–638 (1997)

NUMERICAL SIMULATION OF INCOMPRESSIBLE FLOWS WITH MOVING INTERFACES

MARC MEDALE AND MARC JAEGER

Institut Universitaire des Systèmes Thermiques Industriels, CNRS UMR 139, Technopole de Chateau – Gombert, 13453 Marseille Cedex 13, France

SUMMARY

A numerical model has been developed for the 2D simulation of free surface flows or, more generally speaking, moving interface ones. The bulk fluids on both sides of the interface are taken into account in simulating the incompressible laminar flow state. In the case of heat transfer the whole system, i.e. walls as well as possible obstacles, is considered. This model is based on finite element analysis with an Eulerian approach and an unstructured fixed mesh. A special technique to localize the interface allows its temporal evolution through this mesh. Several numerical examples are presented to demonstrate the capabilities of the model. © 1997 by John Wiley & Sons, Ltd.

KEY WORDS: finite element method; front tracking; incompressible two fluid system; mold filling

1. INTRODUCTION

Some people call flows with moving boundaries free surface flows, others call them moving interface flows. This distinction is made when one or both media on either side of the interface are considered. Determining the interface position in the course of time is one of the main difficulties of these studies. It is, however, advisable to qualify the difficulty level according to the nature of the flow. We can basically outline two types of problems:

1. In the first type, only one parameter, such as height according to a reference plane, can define the interface without ambiguity. We can quote, as an example, maritime and fluvial hydraulic engineering in the environmental sector;
2. In the second type, such as in shaping processes of metals, the geometrical complexity of the interface as well as its evolution requires a more sophisticated treatment.

Our study deals with the second type of problem, for which we have developed a numerical model. This model is based on the finite element method. It was initially developed for modelling the filling of casting moulds,[1] however, as we show herein, the method can be applied more widely. As a thorough bibliographic review can be found in Reference 12, we will only cite in this article the works directly associated with the present study.

First we present the strategy adopted to locate the interface, considering its dominating influence on the structure of the developed model. The total model is then described from the mathematical formulation of the problem to the spatial and temporal discretization. We finally present some examples to assess the model performance as well as a comprehensive simulation example of the filling of a casting mould.

CCC 0271–2091/97/060615–24 $17.50

Received 17 February 1995
Revised 4 August 1996

2. FRONT TRACKING

2.1. Principle of method

The treatment of a problem with a moving boundary, or more generally a moving interface, can be carried out according to a Lagrangian, Eulerian or mixed formulation, leading to very different numerical models.

Finite element analysis, employed extensively in structure calculations, generally uses a Lagrangian kinematics description. Each node of the mesh is associated with a particle of the modelled material(s) and moves with it. The mesh deforms in the course of time (see Figure 1).

However, when the deformation become very large, particularly when touching and near the walls, there is such a distortion in the mesh that singular elements can appear. A remeshing operation is then necessary before proceeding with the computation. Thus it is a particularly efficient and accurate approach to study shaping processes of materials with a certain stiffness, such as extrusion and embossing. However, it rapidly becomes inappropriate, indeed impossible, to apply with less viscous materials.

In fact, the difficulty lies in the mixed characteristics of the problem. The description of the flow implies an Eulerian approach and the tracking of the interface a Lagrangian one. Hence, mixed Eulerian–Lagrangian methods have been developed.[3,4] Their principle is based on a mesh evolution independent of the fluid movement, except in the proximity of the interface where both velocities coincide (see Figure 2).

However, even this approach remains inadequate as soon as the interface becomes too complex geometrically. Besides, it becomes ineffective when facing multiple fronts since, for example, it does not allow a simple treatment of the coalescence phenomenon, i.e. the joining of two fronts or two parts of the same front.

The totally Eulerian approach in which the moving interface is advected through a fixed mesh eliminates any remeshing problem and has been developed for the finite difference method, which can only deal with structured meshes. Here two types of methods can be distinguished: the 'surface-tracking' method and the 'volume-tracking' one. In the first type of method a series of curves represents the interface in a 2D model (see Figure 3(a)). These curves are based on a finite number of points following the moving interfaces. However, it is difficult to apply this method to 3D models because of the vast amount of data to be stored and processed. Furthermore, it still doesn't resolve the question of coalescence. With the second type of method one does not really follow the interface but rather tries to determine in each cell of the mesh the volume fraction taken up by the various fluids (see Figure 3(b)). This procedure allows the treatment of any interface configuration up to approximately a cell in accuracy, however as complex it may be, and allows one to address the coalescence phenomenon. Each fluid present can be identified by introducing particles without mass as tracers.[6] However, the amount of data to be stored and processes is still excessive. In the VOF (volume-of-fluid) technique developed by Hirt and Nichols,[7] the fluid presence or absence at instant t

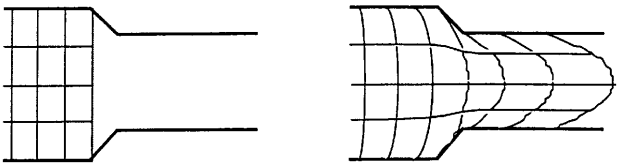

Figure 1. Deformation of mesh in Lagrangian approach

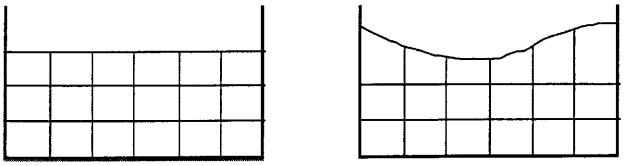

Figure 2. Deformation of mesh in mixed Eulerian–Lagrangian approach

and point (x, y) is characterized by a scalar field $F(x, y, t)$ with value zero (fluid absent) or unity (fluid present). This field is advected by the flow and consequently satisfies the transport equation

$$\frac{\partial F}{\partial t} + \vec{V} \cdot \vec{\nabla} F = 0, \tag{1}$$

where $\vec{V}$ indicates the fluid velocity. The solution of this equation gives the value of the scalar function F at any point of the domain at each instant. The 'filling rate' of a mesh cell can then be easily obtained by integrating. The VOF technique was previously introduced by Hirt and Nichols in the finite difference SOLA algorithm described in Reference 8, using a 'donor–acceptor' technique[9] to solve the transport equation for F.

However, if one wants to utilize the complex geometry capabilities of the finite element method, this technique, i.e. VOF, cannot be considered as it requires the use of meshes with rectangular cells. Unfortunately, the finite element method, like any interpolation-based method, has difficulty in modelling the propagation of a discontinuity accurately. To overcome this difficulty, Thompson[10] introduced the pseudoconcentration method (PCM) to follow an interface between two immiscible fluids. The function F then varies continuously between two extreme values; the points where F takes an index value F_c gives the interface position (see Figure 4(a)).

In fact, this notion of pseudoconcentration function can be extended[11] to any continuous and monotonic scalar field F on the domain with the index value taken on the interface (see Figure 4(b)).

2.2. Cursor concept

The model we have developed is based on the front-tracking technique just described. The problem therefore lies in the solution of the transport equation (1) for a scalar function F initially linear on its domain, but with requirements a little different from the usual ones for a transport problem. Indeed, the accuracy of the computation of F is a crucial parameter only in the neighbourhood of the prescribed value F_c for the interface. Outside this zone, all we have to respect is that F never degenerates to the point of crossing again the F_c-value and rendering problematic the identification of the interface. Of course, a sufficient condition is to preserve the uniqueness character of F during the transport.

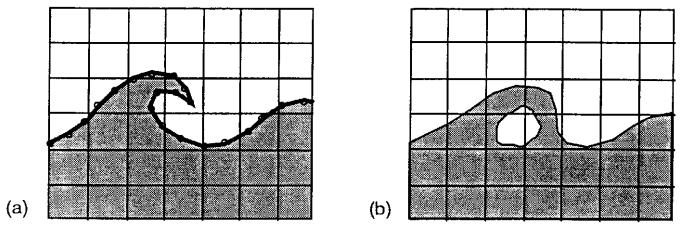

Figure 3. Front tracking in Eulerian approach: (a) line segment method; (b) volume fraction method

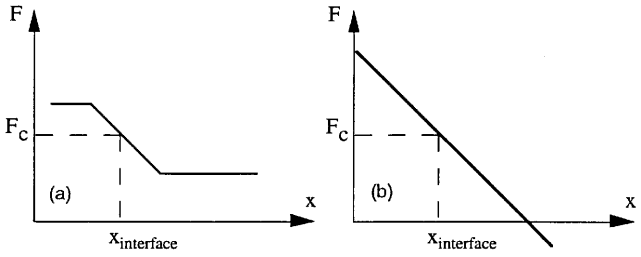

Figure 4. (a) Pseudoconcentration function; (b) generalization

The exact solution of equation (1) can be determined wit the use of characteristics. Indeed, the solution at time step $t + \Delta t$ is given by

$$F(\vec{x}, t + \Delta t) = F(\vec{X}(t), t), \tag{1a}$$

where $\vec{X}(t)$ is the solution of the differential equation defining the characteristic lines,

$$\frac{\mathrm{d}\vec{X}}{\mathrm{d}t} = \vec{V}(\vec{X}(\tau), \tau), \quad t \leqslant \tau \leqslant t + \Delta t, \tag{1b}$$

subject to the final condition $\vec{X}(t + \Delta t) = \vec{x}$.

The analytic solution of the problem can therefore be obtained if one is able to solve the differential equation (1a) exactly. However, this last is non-linear as soon as the velocity field is space-dependent. In this case it is solved up to a given accuracy, whatever the numerical method employed. The idea of a cursor is then to prevent all pollution coming from the transport of F in the region not concerned with the interface evolution. To this end, the resolution of equation (1) is restricted to a narrow band of elements framing the interface and displaying with it at each time step: the cursor (Figure 5).

As illustration, consider the transport of a vertical interface in the 2D convergent/divergent channel of Figure 6(a).

In the context of a 1D model, with an average velocity $U(x)$ deduced from the incompressibility condition (Figure 6b), equation (1b) can be solved analytically. Starting at time t with an ideal

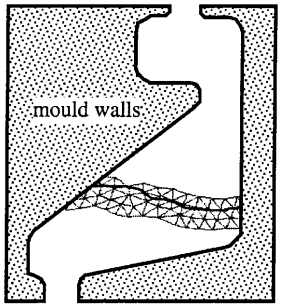

Figure 5. Sketch of interface and its computational cursor in flow domain

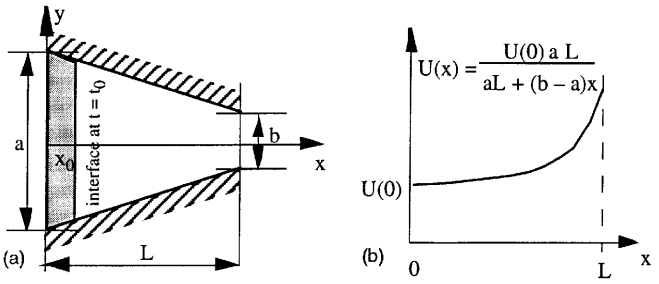

Figure 6. Transport of interface in converging channel: (a) domain; (b) velocity on x-axis

F-profile of shape $F(x,t) = 1 - x, F_c = 0$ being the prescribed value for the interface, the solution provided by (1a) and (1b) for time step $[t, t + \Delta t]$ is

$$F(x, t+\Delta t) = \begin{cases} 1 - \dfrac{aL}{a-b} + \sqrt{\left[\left(x - \dfrac{aL}{a-b}\right)^2 + 2\Delta t U(0)\dfrac{aL}{a-b}\right]} & \text{if } a > b, \\ 1 - \dfrac{aL}{a-b} - \sqrt{\left[\left(x - \dfrac{aL}{a-b}\right)^2 + 2\Delta t U(0)\dfrac{aL}{a-b}\right]} & \text{if } a < b. \end{cases}$$

Note that in order to ensure a real solution for all points in the domain $]0, L]$, the time step value Δt has to respect in the divergent case $(b > a)$ the stability criterion $\Delta t \leqslant aL/U(0)(b-a)$. When a becomes very small, the Lagrangian approach by characteristics can therefore lead to very small time step values, penalizing from the point of view of computational efficiency. This illustrates the limitations of this type of approach for flows presenting some abrupt expansion and, more generally, a separation zone.

In that case the uniqueness of the solution of equation (1b) is no longer ensured. The Eulerian approach on the other hand deals with the solution of the transport equation (1) via a time discretization scheme. We consider for example the explicit Euler scheme which leads to the linear equation

$$F(x, t+\Delta t) = F(x,t) - \Delta t U(x) \left.\frac{\partial F}{\partial x}\right|_{(x,t)},$$

since its solution is obvious:

$$F(x, t+\Delta t) = 1 - x + \Delta t U(0) \frac{aL}{aL + (b-a)x}.$$

This solution is plotted in Figure 7 after the first time step and is compared with the analytic one given by the Lagrangian approach in the convergent case $(L = 10, a = 11, b = 1)$ with an inlet velocity of $U(0) = 1$ and a time step value $\Delta t = 1$.

One notes immediately that for this value of the time step the transport is correctly represented near the interface. On the other hand, it is very badly taken into account near the exit, even making a false interface appear. Thus we see the usefulness of the cursor, which allows the elimination of this zone from the domain of interest when the interface is located near the entrance of the duct.

From a physical point of view, since the scalar field F is purely advected by the flow, its initial distribution is simply translated along the characteristic lines as long as the velocity field is uniform. However, if gradients appear in the velocity field, the initial distribution undergoes in addition to that translation a distortion whose amplitude depends on the velocity gradients. Therefore the basic idea of the cursor consists of restricting the front advection problem to its minimal part around the

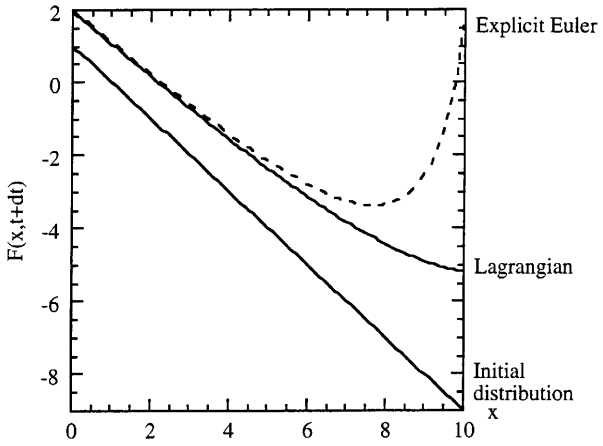

Figure 7. Advection of F-field in converging channel

interface in order to reduce this distortion. In doing this, the narrower the cursor across the characteristic lines around the interface is, the more the velocity variations on that stripe are reduced and the more the distortion of the F-profile is reduced.

From the numerical point of view the error introduced by the explicit Euler scheme can be analyzed in seeking which approximations this scheme comes down to using in equations (1a) and (1b). To this end we can expand the left-hand side of (1a) in a Taylor series at point x, with $\Delta\vec{X} = \vec{x} - \vec{X}(t)$:

$$F(\vec{x}, t + \Delta t) = F(\vec{x} - \Delta\vec{X}, t) = F(\vec{x}, t) - \Delta X_i \left.\frac{\partial F}{\partial x_i}\right|_{(x,t)} + \frac{\Delta X_i \Delta X_j}{2} \left.\frac{\partial^2 F}{\partial x_i \partial x_j}\right|_{(x,t)} + \cdots.$$

The explicit Euler scheme is obtained from this expansion restricted to first order and with the approximation $\Delta\vec{X} = \Delta t\vec{V}(\vec{x}, t)$ of the solution of equation (1b). Note that the second-order Taylor–Galerkin scheme TG2 advocated by Lewis *et al.*[12] can be deduced from the same approximation of Δx but with the expansion extended to second order. However, in the setting of our example these two schemes are identical, since at initial time t the F-field is linear. Thus, the use of a second-order scheme indeed improves the accuracy with which the field is transported, but it does not permit one to overcome the problem of a possible false interface.

In fact, the idea of focusing the front tracking on the interface neighbourhood is implicitly included in the initial PCM of Thompson.[10] Indeed, the pseudoconcentration function admits gradients only near the interface and is flat (zero gradient) outside this region. However, one can expect that this shape will not be conserved during the computation owing to the numerical scheme. Moreover, numerical oscillations in the vicinity of the slope discontinuity could be generated.[13] The cursor concept is a convenient way to overcome these difficulties since it restricts the computation to non-zero-gradient regions.

2.3. Cursor update

In an Eulerian approach the initial mesh stretches on the whole fluid flow domain. Nevertheless, only few elements of this initial mesh that overlie the interesting regions of the front advection problem are selected to make up the cursor (see Figure 8(a)). Therefore the computation domain of interest for this problem is restricted to the cursor. After the new front position has been identified

(see Figure 8(b)), the update of the cursor with respect to this position consists of a two-stage sequence (see Figure 8(c)).

1. Select as previously mentioned the elements that make up the cursor; that is, where requested, discard useless upwind elements and add new ones in the downwind direction. The cursor width is defined through the minimum and maximum values of F, which must be specified. Since for an interface one can encounter segments moving forwards and others backwards, or moving forwards at one time step and backwards at another one, a symmetric cursor with respect to the interface is provided. Typically in our applications we use a cursor about five elements wide.
2. Initialize the nodes of elements entering the cursor and where the F-function has not yet been computed during the previous time step. Recall that this last aspect has to be considered in our model since the standard finite element space discretization yields a central scheme.

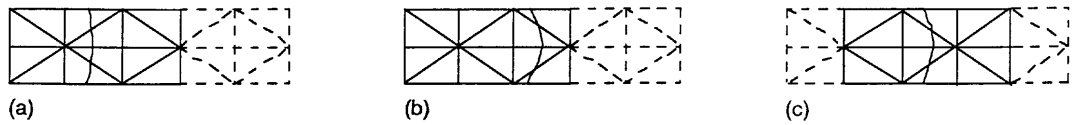

Figure 8(a)–(c)

This initialization procedure consists of extending the function $F(x, y, t)$ along the characteristic lines going down those nodes, according to the initial slope.

2.4. Control of mass conservation

With the front-tracking strategy previously described, based on a pseudoconcentration function, the conservation of mass of all real fluids is not ensured. To illustrate this point, consider for example the reattachment of two portions of the same interface. With our model this phenomenon can be simulated only up to the level of the element size. As the interface moves, the value of the F-function becomes greater than the index value F_c at all nodes encountered during this displacement. When all nodes of an element have their F-value greater than F_c, this element is seen as a filled element. It follows that the model is not able to distinguish between a filled element and one that is crossed twice by the interface. In this way, mass could be artificially created or lost.

In some applications, mass conservation can be a priority. For these cases we have developed a control procedure based on a global mass balance for the system. The quantity of each fluid in the domain (deduced from the scalar field F) must be consistent with the mass fluxes at the inlet and outlet boundaries. If this balance is not satisfied, a correction of the interface position is carried out by slightly modifying the index value F_c. This control procedure results in a spreading over the whole interface of the errors introduced in some specific regions of it. When the mesh used is coherent with the complexity of the flow pattern, the correction needed for F_c and consequently the change in the interface position are almost very small. In this case the mass conservation control procedure influences only slightly the front tracking. However, it eliminates the accumulation in time of mass deficit or gain.

Finally, the complete procedure of interface localization is achieved according to the algorithm in Figure 8(d).

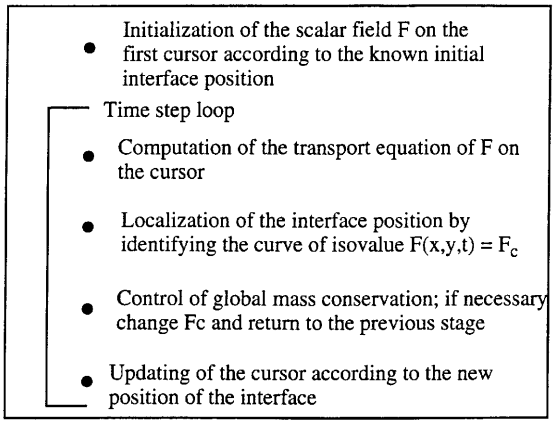

Figure 8(d). Interface localization algorithm

3. NUMERICAL MODEL

3.1. Transport equation of the interface

The above strategy to localize the interface (or interfaces if there are multiple fronts) is based on the transport of a scalar field F. Mathematically speaking, the first-order hyperbolic equation (1) describes the purely convective transport of F. In a 2D Cartesian co-ordinate system it is

$$\frac{\partial F}{\partial t} + U\frac{\partial F}{\partial x} + V\frac{\partial F}{\partial y} = 0, \tag{2}$$

where U and V are respectively the x- and y-component of the velocity vector $\vec{V}$.

This equation has to be solved at each time step on the variable domain D_F corresponding to the cursor with a Dirichlet boundary condition on the inlet boundary. The initial value of the function F is specified on the cursor and is a linearly decreasing function of space. As the slope has been fixed, this distribution is obtained by associating the also fixed index value F_c with the initial position of the interface.

3.2. Equations governing fluid flow

In theory it is only necessary to know the velocity of the points on the interface in order to transport it. This knowledge is acquired by determining the flow of one of the fluids present. In this case the interface is considered as a surface free from any dynamic action of the fluid on the other side of the interface. However, in many situations this action cannot be neglected, e.g. flows in confined media (e.g. filling of moulds in the casting industry) where the walls strongly influence the flow of the various fluids. The resulting excess pressure or recirculation areas then play an important role in the interface evolution, no matter what side they occur on.

That is why in the model we have developed we determine the flow of all fluids present, i.e. we are considering a two-fluid system. On the macroscopic scale the variation in the physical properties is very rapid and corresponds to a discontinuity when passing the interface. Nevertheless, the numerical model cannot represent the interface exactly since it crosses elements of the mesh. In fact, in the proximity of the interface we can identify three regions with different material properties. The first two correspond to the elements occupied only by one or the other of the two fluids, while the third corresponds to the band of elements crossed by the interface (transition elements), to which we assign specific properties. These properties are the average of the properties of the two fluids situated on

either side. The result is a diffuse representation of the interface since the mesh is coarse. As far as the viscosity assigned to the transition elements is concerned, a value slightly larger than the average is generally necessary to stabilize the interface (i.e. damping of surface waves). This artificial increase in the viscosity in a way replaces the stabilizing effect of the surface tension which has been neglected in the present model. Note that in such an approach where we take into account the wholeness of the materials located on both sides of the interface, no additional boundary condition has to be imposed on the interface.

Finally, as all the fluids present are assumed incompressible, the flow can be determined by the solution of the Navier–Stokes equations with mechanical properties specific to each region previously described (density ρ_α and dynamic viscosity μ_α, where a different index α is associated with each region). In a 2D model these equations take the following form in a Cartesian co-ordinate system (x, y):

$$\rho_\alpha\left(\frac{\partial U}{\partial t}+U\frac{\partial U}{\partial x}+V\frac{\partial U}{\partial y}\right)=-\frac{\partial P}{\partial x}+\mu_\alpha\left(\frac{\partial^2 U}{\partial x^2}+\frac{\partial^2 U}{\partial y^2}\right)+f_x^{\mathrm{vol}}, \tag{3}$$

$$\rho_\alpha\left(\frac{\partial V}{\partial t}+U\frac{\partial V}{\partial x}+V\frac{\partial V}{\partial y}\right)=-\frac{\partial P}{\partial y}+\mu_\alpha\left(\frac{\partial^2 V}{\partial x^2}+\frac{\partial^2 V}{\partial y^2}\right)+f_y^{\mathrm{vol}}, \tag{4}$$

$$\frac{\partial U}{\partial x}+\frac{\partial V}{\partial y}=0, \tag{5}$$

where t represents time, U and V represent the velocity components with respect to x and y respectively, f_x^{vol} and f_y^{vol} are the components of the body force and P is the pressure.

3.3. Equation governing heat transfer

A study of heat transfer can be performed on all the whole fluids present since the velocity field for each of them is known; heat transfer in the solid parts of the system, such as the walls of a mould, can also be studied. The introduction of empirical exchange coefficients can thus be avoided at the internal walls of the system as well as on the moving interface. To study heat transfer, we must solve the heat equation in a domain whose regions have different thermal properties (specific heat C_{p_α} and thermal conductivity k_α). In a 2D Cartesian co-ordinate system (x, y) this equation takes the form

$$\rho_\alpha C_{\mathrm{p}_\alpha}\left(\frac{\partial T}{\partial t}+U\frac{\partial T}{\partial x}+V\frac{\partial T}{\partial y}\right)=k_\alpha\left(\frac{\partial^2 T}{\partial x_2}+\frac{\partial^2 T}{\partial y^2}\right), \tag{6}$$

where T indicates the temperature.

Note that in those regions occupied by solid materials (considered to have constant shape) the energy equation is just the transient heat conduction equation since the convection terms are zero. As for the region corresponding to the element band crossed by the interface, we assign thermal properties which are the average of the properties of the two fluids on both sides. From a thermal point of view it is also a diffuse representation of the interface whose accuracy is governed by the element size.

3.4. Solution strategy

The three problems we have just described are strongly coupled as illustrated in Figure 9.

The interface position and its physical properties can play a crucial role in both fluid mechanics and heat transfer problems. Conversely, the velocity field must be known to locate the interface and to study heat transfer. The temperature field can only influence the flow if the physical properties are temperature-dependent. In particular, a local change in density can induce natural convection; to take

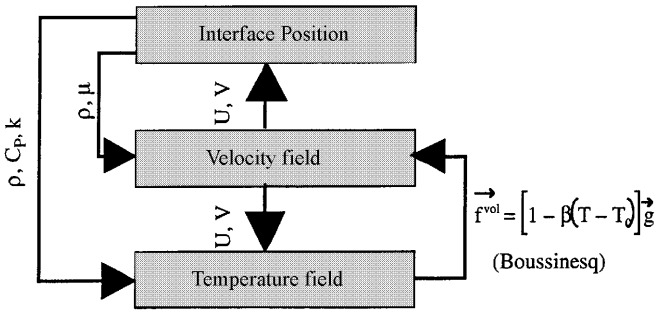

Figure 9. Schematic diagram of various interactions between the three physical problems

this phenomenon into account, we have chosen simplified Boussinesq modelling in which the density variation is considered only in the body force of the Navier–Stokes equations. Thus, if gravity is the only body force, the expression of this force is taken to be

$$\vec{f^{\text{vol}}} = \rho_\alpha[1 - \beta_\alpha(T - T_0)]\vec{g}, \tag{7}$$

where β_α is the coefficient of volume expansion of fluid α, ρ_α is its density at the reference temperature T_0 and $\vec{g}$ is the gravity vector. Presently the model does not consider any other temperature variation in other physical properties.

The traditional finite element method consists of solving the three problems simultaneously, i.e. with the explicit consideration of the coupling in the system. However, our previous CFD experience using the finite element method[14] led us to revise this strategy. Indeed, in addition to the problem of fluid mechanics, there are generally several transport problems (heat, concentration, turbulence, etc.). Segregated computation of each problem is advantageous for numerical efficiency, since it leads to a sequence of systems of reduced size, and for the development as well. Each problem is solved independently with the best-adapted numerical scheme. The coupling between the problems must then be taken into account with a coupling algorithm such as the famous SIMPLE procedure in finite differences and finite volumes.[15] In the present study this leads to the algorithm of Figure 10 where each problem is solved only once at each time step.

The system to be solved for each problem is generated according to the usual techniques used in the finite element method;[16] that is, an integral formulation of the problem is discretized spatially according to a finite element approximation and temporally according to the first-order implicit Euler scheme.

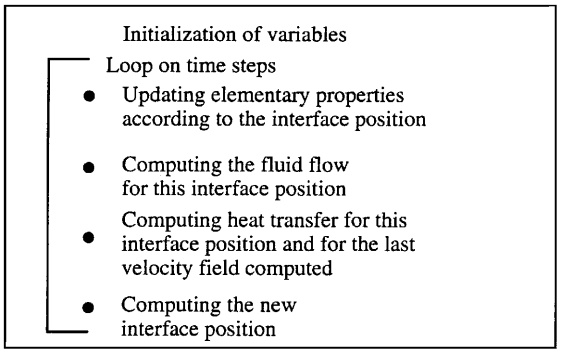

Figure 10. Solution algorithm

3.5. Finite element model of interface advection

The weighted residual method applied to the transport equation (2) of the interface leads to the integral form

$$I_{\mathrm{F}} = \int_{D_{\mathrm{F}}} \delta F \left(\frac{\partial F}{\partial t} + \mathrm{U} \frac{\partial F}{\partial x} + \mathrm{V} \frac{\partial F}{\partial y} \right) \mathrm{d}s = 0 \tag{8}$$

on the domain D_{F} associated with the cursor for an arbitrary admissible test function $\delta F(x, y)$.

For the spatial discretization we have selected the Lagrangian triangular isoparametric element with three nodes. The approximation of the admissible functions $F(x, y, t)$ and $\delta F(x, y)$ is therefore piecewise linear and continuous on D_{F}, sufficient for the integral form I_{F} to exist. Denoting by ϕ_i the shape functions associated with this discretization, the approximation by the admissible functions on the domain D_{F} is

$$F(x, y, t) = \sum_{i=1}^{N_F} \phi_i(x, y) F_i(t), \qquad \delta F(x, y) = \sum_{i=1}^{N_F} \phi_i(x, y) \delta F_i, \tag{9}$$

where $F_i(t)$ and δF_i are the values at instant t taken by the functions F and δF at node i and N_{F} indicates the total number of nodes in the cursor.

The introduction of this approximation in the integral form I_{F} leads to the system of ordinary differential equations

$$[M^{\mathrm{F}}]\{\dot{F}\}_t + [K^{\mathrm{F}}]\{F\}_t = \{0\}, \tag{10}$$

where the N_{F} nodal values $F_i(t)$ as well as their temporal derivatives $\dot{F}_i(t)$ have been organized into the vectors $\{F\}_t$ and $\{\dot{F}\}_t$ respectively. The matrices $[M^{\mathrm{F}}]$ and $[K^{\mathrm{F}}]$ are given by

$$M_{ij}^{\mathrm{F}} = \int_{D_{\mathrm{F}}} \phi_i \phi_j \, \mathrm{d}s, \qquad K_{ij}^{\mathrm{F}} = \int_{D_{\mathrm{F}}} \phi_i \left(U \frac{\partial \phi_j}{\partial x} + V \frac{\partial \phi_j}{\partial y} \right) \mathrm{d}s. \tag{11}$$

Utilizing implicit Euler time integration leads finally to the following algebraic system at each time step:

$$([M^{\mathrm{F}}] + \Delta t [K^{\mathrm{F}}])\{F\}_t = [M^{\mathrm{F}}]\{F\}_{t-\Delta t}. \tag{12}$$

3.6. Finite element model of heat transfer problem

The weighted residual method applied to the energy equation (6) leads to the integral form

$$I_{\mathrm{T}} = \int_{D_{\mathrm{T}}} \rho_\alpha C_{p_\alpha} \delta T \left(\frac{\partial T}{\partial t} + U \frac{\partial T}{\partial x} + V \frac{\partial T}{\partial y} \right) \mathrm{d}s + \int_{D_{\mathrm{T}}} k_\alpha \left(\frac{\partial \delta T}{\partial x} \frac{\partial T}{\partial x} + \frac{\partial \delta T}{\partial y} \frac{\partial T}{\partial y} \right) \mathrm{d}s - \int_{\partial D_{\mathrm{T}}} k_\alpha \delta T \frac{\partial T}{\partial n} \, \mathrm{d}l = 0 \tag{13}$$

on the domain D_{T} of this problem for an arbitrary admissible test function $\delta T(x, y)$. Note that the diffusion terms have been integrated by parts, making an integral appear on the domain boundary ∂D_{T} with outer normal $\vec{n}$. When considering only isothermal or adiabatic boundary conditions, this boundary integral cancels itself. For the spatial discretization we have selected the same element as previously mentioned for F. The approximation by admissible functions on the domain D_{T} is

$$T(x, y, t) = \sum_{i=1}^{N_T} \phi_i(x, y) T_i(t), \qquad \delta T(x, y) = \sum_{i=1}^{N_T} \phi_i(x, y) \delta T_i, \tag{14}$$

where $T_i(t)$ and δT_i are the values taken by the functions T and δT at node i and instant t. N_T indicates the total number of nodes of the mesh used for this problem.

With implicit Euler time integration the algebraic system to be solved at each time step is written finally as

$$([M^T] + \Delta t[K^T])\{T\}_t = [M^T]\{T\}_{t-\Delta t}, \tag{15}$$

with matrices $[M^T]$ and $[K^T]$ defined by

$$M_{ij}^T = \int_{D_T} \rho_\alpha C_{p_\alpha} \phi_i \phi_j \, \mathrm{ds}, \tag{16}$$

$$K_{ij}^T = \int_{D_T} \rho_\alpha C_{p_\alpha} \phi_i \left(U \frac{\partial \phi_j}{\partial x} + V \frac{\partial \phi_j}{\partial y} \right) \mathrm{ds} + \int_{D_T} k_\alpha \left(\frac{\partial \phi_i}{\partial x}\frac{\partial \phi_j}{\partial x} + \frac{\partial \phi_i}{\partial y}\frac{\partial \phi_j}{\partial y} \right) \mathrm{ds}. \tag{17}$$

Note that boundary conditions other than isothermal or adiabatic ones can be specified easily by considering specific boundary elements (convection, radiation, etc.).[17]

3.7. Finite element model of flow problem

The weighted residual method applied to the equation system (3)–(5) describing the flow leads to the integral form

$$\begin{aligned} I_v = & \int_{D_v} \delta U \left[\rho_\alpha \left(\frac{\partial U}{\partial t} + U \frac{\partial U}{\partial x} + V \frac{\partial U}{\partial y} \right) + \frac{\partial P}{\partial x} - f_x^{\mathrm{vol}} \right] \mathrm{ds} \\ & + \int_{D_v} \delta V \left[\rho_\alpha \left(\frac{\partial V}{\partial t} + U \frac{\partial V}{\partial x} + V \frac{\partial V}{\partial y} \right) + \frac{\partial P}{\partial y} - f_y^{\mathrm{vol}} \right] \mathrm{ds} \\ & + \int_D \delta P \left(\frac{\partial U}{\partial x} + \frac{\partial V}{\partial y} - \frac{P}{\lambda} \right) \mathrm{ds} + \int_{D_v} \mu_\alpha \left(\frac{\partial \delta U}{\partial x}\frac{\partial U}{\partial x} + \frac{\partial \delta U}{\partial y}\frac{\partial U}{\partial y} + \frac{\partial \delta V}{\partial x}\frac{\partial V}{\partial x} + \frac{\partial \delta V}{\partial y}\frac{\partial V}{\partial y} \right) \mathrm{ds} \\ & - \int_{\partial D_v} \mu_\alpha \left(\delta U_n \frac{\partial U_n}{\partial n} + \delta U_{tg} \frac{\partial U_{tg}}{\partial n} \right) \mathrm{d}l = 0 \end{aligned}$$

on the domain D_V for arbitrary admissible test functions $\delta U(x, y)$, $\delta V(x, y)$ and $\delta P(x, y)$. The diffusion terms have been integrated by parts, making an integral appear on the boundary ∂D_v of the domain D_v. The velocity is expressed as in a normal component U_n and a tangential component U_{tg} at the boundary ∂D_V, while $\vec{n}$ indicates the outer normal. This boundary integral does not appear for homogeneous Dirichlet or Neumann boundary conditions. In general it allows us to take into account the wall shear stress through the introduction of a specific boundary element.[1]

Note also that we resort to a penalty formulation of the incompressibility constraint,[18] i.e. the continuity equation is replaced by

$$\frac{\partial U}{\partial x} + \frac{\partial V}{\partial y} - \frac{P}{\lambda} = 0, \tag{5a}$$

where λ is the penalty coefficient ($\lambda \approx 10^8$).

The spatial discretization is a bit more complicated than those of both the previous problems. Indeed, an approximation that is identical for velocities and pressure leads to an unstable numerical scheme. This problem of incompatibility between an approximation spaces of velocities and pressure is expressed mathematically by a stability condition 'inf-sup'.[19–21] The six-node triangular element (see Figure 11) originally developed by Bercovier and Pironneau[22] satisfies this criterion. It provides a linear approximation of pressure on the whole element and a linear approximation of velocities on each of the four three-node triangles within the element. We have selected it for our model because of

its numerical efficiency. Indeed, as for the three-node triangular element used for the temperature field and interface evolution, it does not require any Gaussian numerical integration. In fact, this element can be regarded as a macroelement made up of four three-node triangular elements identical with those used for the function F and the temperature T. However, the middle nodes must be positioned absolutely in the centre of the three sides. The pressure can then be eliminated from these three nodes by demanding a linear approximation on each side. This results in a linear approximation on the whole macroelement T6 (see Figure 11).

Shape functions associated with the velocity approximation are consequently the same as for the function F and the temperature T. Denoting by ψ_i the shape functions for pressure, the approximation by admissible functions on the domain D_V is then defined by

$$U(x,y,t)=\sum_{i=1}^{N_v}\phi_i(x,y)U_i(t), \qquad \delta U(x,y)=\sum_{i=1}^{N_v}\phi_i(x,y)\delta U_i, \tag{19}$$

$$V(x,y,t)=\sum_{i=1}^{N_v}\phi_i(x,y)V_i(t), \qquad \delta V(x,y)=\sum_{i=1}^{N_v}\phi_i(x,y)\delta V_i, \tag{20}$$

$$P(x,y,t)=\sum_{i=1}^{N_p}\psi_i(x,y)P_i(t), \qquad \delta P(x,y)=\sum_{i=1}^{N_p}\psi_i(x,y)\delta P_i, \tag{21}$$

where N_V and N_P indicate the number of nodes for velocities and pressure respectively.

With implicit Euler temporal discretization the algebraic system to be solved at each time step is finally

$$([M]+\Delta t[K])\begin{Bmatrix}\{U\}_t\\ \{V\}_t\\ \{P\}_t\end{Bmatrix}=[M]\begin{Bmatrix}\{U\}_{t-\Delta t}\\ \{V\}_{t-\Delta t}\\ \{P\}_{t-\Delta t}\end{Bmatrix}+\Delta t\begin{Bmatrix}\{F^U\}_t\\ \{F^V\}_t\\ \{0\}\end{Bmatrix}, \tag{22}$$

where

$$[M]=\begin{bmatrix}[M^U] & [0] & [0]\\ [0] & [M^V] & [0]\\ [0] & [0] & [0]\end{bmatrix}, \qquad [K]=\begin{bmatrix}[K^U] & [0] & [K^{UP}]\\ [0] & [K^V] & [K^{VP}]\\ [K^{PU}] & [K^{PV}] & [K^P]\end{bmatrix}.$$

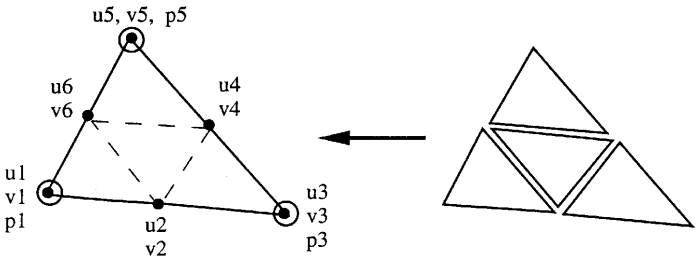

Figure 11. Finite element for computing velocity and pressure fields

The various matrices involved in the system are defined by

$$M_{ij}^{\mathrm{U}} = M_{ij}^{\mathrm{V}} = \int_{D_{\mathrm{V}}} \rho_\alpha \phi_i \phi_j \mathrm{d}s, \tag{23}$$

$$K_{ij}^{\mathrm{U}} = K_{ij}^{\mathrm{V}} = \int_{D_{\mathrm{V}}} \rho_\alpha \phi_i \left(U \frac{\partial \phi_j}{\partial x} + V \frac{\partial \phi_j}{\partial y} \right) \mathrm{d}s + \int_{D_{\mathrm{V}}} \mu_\alpha \left(\frac{\partial \phi_i}{\partial x} \frac{\partial \phi_j}{\partial x} + \frac{\partial \phi_i}{\partial y} \frac{\partial \phi_j}{\partial y} \right) \mathrm{d}s, \tag{24}$$

$$\begin{aligned} K_{ij}^{\mathrm{UP}} &= \int_{D\mathrm{v}} \phi_i \frac{\partial \psi}{\partial x} \, \mathrm{d}s, \qquad K_{ij}^{\mathrm{VP}} = \int_{D_{\mathrm{V}}} \phi_i \frac{\partial \psi_j}{\partial y} \, \mathrm{d}s, \\ K_{ij}^{\mathrm{PU}} &= \int_{D_{\mathrm{V}}} \psi_i \frac{\partial \phi_j}{\partial x} \, \mathrm{d}s, \qquad K_{ij}^{\mathrm{PV}} = \int_{D_{\mathrm{V}}} \psi_i \frac{\partial \phi_j}{\partial y} \, \mathrm{d}s, \qquad K_{ij}^{\mathrm{P}} = -\frac{1}{\lambda} \int_{D\mathrm{V}} \psi_i \psi_j \, \mathrm{d}s. \end{aligned} \tag{25}$$

Body forces such as centrifugal, Coriolis and gravity forces also lead to a matrix contribution to $[K]$. Here we have only considered a buoyancy force in which gravity has a y-component. The loading vectors using the Boussinesq approximation are

$$F_i^{\mathrm{U}} = 0, \qquad F_i^{\mathrm{V}} = -\int_{D_{\mathrm{V}}} \rho_\alpha [1 - \beta_\alpha (T - T_0)] g \phi_i \mathrm{d}s. \tag{26}$$

4. APPLICATIONS

4.1. Flow in a T-branch

The first example illustrates the model in the case of flow configurations with multiple interfaces. In this study we consider two distinct interfaces at the initial instant. The flow conditions chosen within the branch illustrates three typical stages in interface evolution:

(a) transport of distinct interfaces
(b) joining of the two interfaces
(c) formation of a common interface

The domain has the geometrical form of a T-branch (see Figure 12(a)) which is symmetrical to the line IJ. The fluid enters the domain at sections AB and EF with perfectly identical flow conditions. This allows one to obtain two identical flows converging towards the common outlet section indicated by CD.

The finite element covering of the domain consists of 224 triangular elements with six nodes (see Figure 12(b)) to which correspond 433 nodes.

Fluid flow. In this example we focus our interest on the transport and evolution of the interfaces in the domain. Thus we assume that the flow remains independent of the interface position and steady. Therefore it is calculated only once. The flow-driving force in this problem is a pressure gradient imposed between the inlet sections and the outlet one. The boundary conditions selected to determine the flow in this system are the following.

1. On the inlet sections AB and EF: $P = \bar{P}_1$.
2. On the outlet section CD: $P = \bar{P}_2$ ($\bar{P}_1 - \bar{P}_2 = 12 \times 10^5$ Pa).
3. The normal velocity component U_{n} is set to zero on the walls BC, DE and FA.

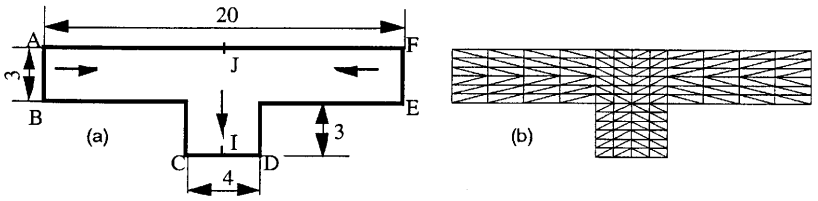

Figure 12. Transport of multiple interfaces: (a) geometry of problem; (b) spatial discretization of flow domain

4. A wall shear stress defined by $\tau_p = -\alpha U_{tg}$ is applied to the same contours (BC, DE and FA). The coefficient of friction is set to $\alpha = 0{\cdot}01$, while U_{tg} indicates the tangential slide velocity of the fluid.

The steady state fluid flow obtained under these conditions is presented in Figure 13.

Interface transport and localization. There are two interfaces inside the domain, symmetrically located considering their respective inlet sections. Therefore the initial distribution of the function F on the computational domain is based on setting up two cursors, each one surrounding an interface:

$$\begin{aligned} &\rightarrow \quad -10 \leqslant x \leqslant -8, \quad F(x, y, t_0) = -9 - x \\ &\rightarrow \quad -8 \leqslant x \leqslant 8, \quad F(x, y, t_0) = -1 \\ &\rightarrow \quad 8 \leqslant x \leqslant 10, \quad F(x, y, t_0) = -9 + x \end{aligned}$$

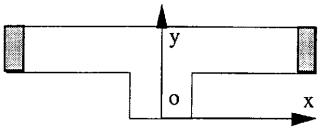

Both interfaces shall be defined at each instant of time by the same index value $F_c = 0$. A cursor is automatically put around the current position of each interface. It is made up of elements of the mesh whose nodal value of the function F belongs to the interval $]1, -1[$. Thus, during the first steps, both cursors move towards one another in the domain, as also do the interfaces which they surround. As soon as they meet each other, they constitute only one cursor which surrounds both interfaces.

A Dirichlet boundary condition is applied on inlet sections AB and EF, i.e. $F(-10, y, t) = F(10, y, t) = 1$. The evolution of the interface position in the flow is described in Figure 14.

4.2. Broken dam problem

A rectangular column of water in hydrostatic equilibrium is initially confined between two vertical walls. The water column is one unit wide and two units high. It is submitted to a gravity field acting downwards with $g' = 0{\cdot}01$ m s^{-2} magnitude in order to diminish turbulence effects such as breaking. At the beginning of the calculation the right wall (dam) is removed and water is allowed to flow out along a dry horizontal floor.

The test case is interesting to check on the capability of the numerical model and to compare with results reported in the literature.[7,23] It also exhibits interesting physical and numerical features in the way it raises a few questions.

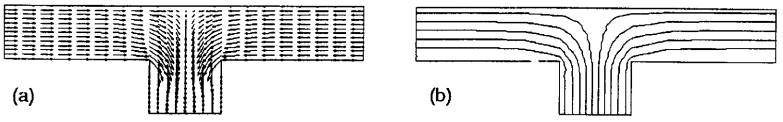

Figure 13. Steady stateflow in T-branch: (a) velocity field; (b) streamlines

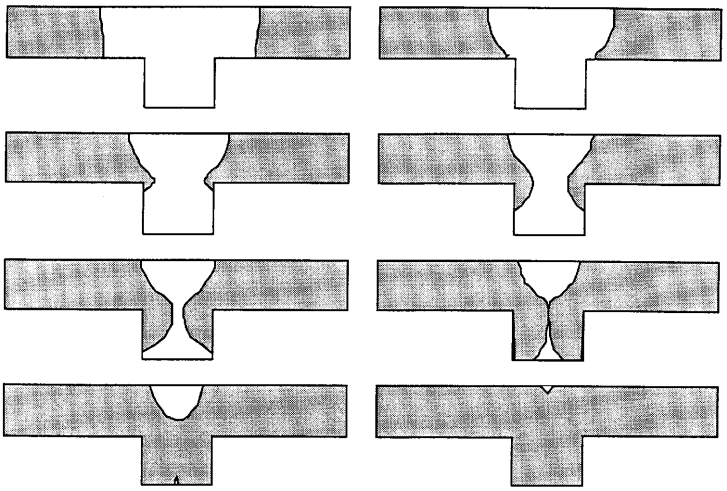

Figure 14. Positions of interfaces at various instants

1. Which boundary conditions have to be imposed on the top and right parts of the computational domain?
2. How does the air flow influence the water flow?

Numerical computations. The computational domain is extended to six times the width of the column in the horizontal direction ($0 \leqslant x \leqslant 6$) and twice its height in the vertical direction ($0 \leqslant 4y \leqslant 4$). In doing this, we wish to limit the influence of the boundary conditions acting on the upper and right parts of the computational domain. We have performed our calculations with two meshes built on 6161 nodes and 3000 elements for the finer one and 4641 nodes and 2250 elements for the coarser one.

Fluid flow. The two fluids considered in this example are water (density $\rho_1 = 1000$ kg m^{-3} and dynamic viscosity $\mu_1 = 10^{-3}$ Pa s) and air (density $\rho_2 = 1$ kg m^{-3} and dynamic viscosity $\mu_2 = 10^{-5}$ Pa s).

Concerning the boundary conditions on the left and bottom parts of the computational domain, we imposed the normal component of the velocity to be zero ($U_n = 0$) and also applied the free slip condition ($\partial U_{tg}/\partial n = 0$) on these parts of the boundary. Dealing now with the upper and right parts of the computational domain, we have experimented with two types of boundary conditions. These parts were first considered as open boundaries and consequently we imposed the associated boundary conditions $\partial U_n/\partial n = 0$ and $\partial U_{tg}/\partial n = 0$. In a second stage we considered these two boundaries as walls and therefore imposed the boundary conditions $U_n = 0$ and $\partial U_{tg}/\partial n = 0$. The pressure was prescribed as zero at the upper right corner of the computational domain for both cases.

The initial solution of the velocity components is set to zero over the entire domain, while the pressure satisfies the hydrostatic equilibrium.

Transport and localization of interface. The initial distribution of the function F on the computational domain is designed to satisfy $F_0(x, y) = F_c = 0$ at the initial interface location. This initial distribution is performed as: if $0 \leqslant y \leqslant 1 + x \leqslant 4$, then $F_0(x, y) = x - 1$, else $F_0(x, y) = y - 2$.

Results. We have plotted in Figure 15 the location of the leading edge of the water–air interface versus non-dimensional time ($t' = t\sqrt{(2g'/a)}$ from experimental results[23] and from our various numerical results.

Owing to the fact we simulate the flow of both fluids (air and water) in the whole domain, it is clear that the boundary condition on the right part of the computational domain influences the whole flow and consequently the interface location. One can see from Figure 15 that the second type of boundary condition (confined domain) fits the experimental results better, except when the leading edge of the front is getting closer and closer to the right wall. The reason comes from the fact that in the late stage of spreading, the leading edge of the interface reaches the region where the flow moves up along the right wall of the confined domain. Therefore it cannot spread any further as it did in the previous stage. Nevertheless, both numerical results agree reasonably well with the experimental behaviour.

One can get a more global description of the spreading sequence in Figure 16, where a few interface locations are drawn at selected non-dimensional times.

The amount of computational work required to get the leading edge of water at $x = 4{\cdot}0$ is 765 min (on a Sun Sparc 10–51) for the finer mesh but only 425 min for the coarser one.

4.3. *Free surface flow with obstacle*

This example is used to evaluate the action of the flow on the interface position and vice versa. Indeed, when the fluids separated by the interface have very different physical properties (e.g. liquid metal and air), the interface position can have a pronounced effect on the flow.

The initial interface position separating liquid metal and air in the flow domain defines the initial configuration of the problem. The shape is vertical at a given distance from the inlet section AB (see Figure 17(a)) and defines at this initial instant a fixed column of liquid metal.

The simulation starts when an injection velocity is imposed on the inlet section (AB) of the mould. This velocity is imposed as a flat profile of constant magnitude over the section AB. Consequently, during the filling phase the liquid metal is subjected to (a) an imposed flow on the inlet section (AB) and (b) a gravity field which acts downwards perpendicular to the inlet velocity.

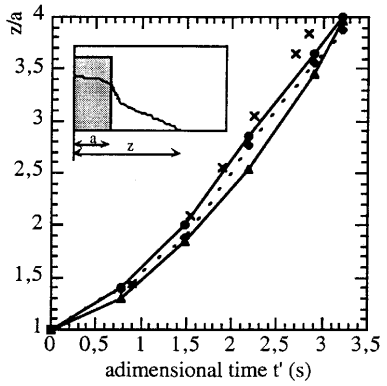

Figure 15. Comparison of calculated results with experimental data: ×, experimental data; —●—, fine mesh with confined domain; - -◆- -, coarse mesh with confined domain; —▲—, fine mesh with open boundary domain

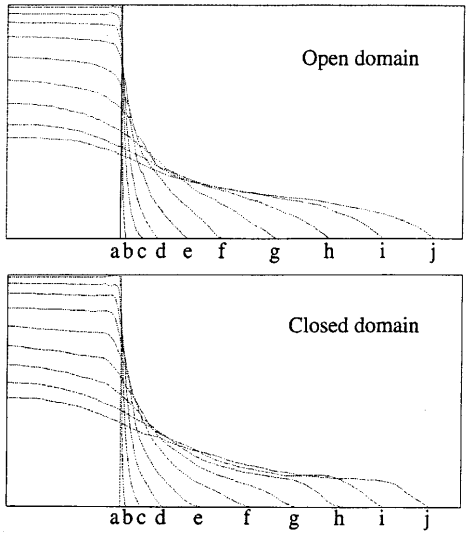

Figure 16. Interface locations at selected non-dimensional times for finer mesh: a, $t=0{\cdot}0$ s; b, $t=0{\cdot}3$ s; c, $t=0{\cdot}6$ s; d, $t=0{\cdot}9$ s; e, $t=1{\cdot}2$ s; f, $t=1{\cdot}5$ s; g, $t=1{\cdot}8$ s; h, $t=2{\cdot}1$ s; i, $t=2{\cdot}4$ s; j, $t=2{\cdot}7$ s

The mesh of the domain is composed of 689 nodes and 364 elements (312 T6 elements in the domain and 52 elements along the solid walls; see Figure 17(b)).

Fluid flow. The two fluids are liquid cast iron (density $\rho_1 = 6500$ kg m^{-3} and dynamic viscosity $\mu_1 = 2 \times 10^{-2}$ Pa s) and air (density $\rho_2 = 1{\cdot}2$ kg m^{-3} and dynamic viscosity $\mu_2 = 2 \times 10^{-5}$ Pa s). The boundary conditions are as follows.

1. On AB: $U = 0{\cdot}1$ m s^{-1} and $V = 0$.
2. On BCDE and FGHA: $U_n = 0$ and $\tau = -\alpha U_{tg}$, with $\alpha = 0{\cdot}01$.
3. On EF: $\partial U_n / \partial n = 0$.
4. At F: $P = 0$.

The initial solution is chosen as zero for the flow variables over the entire domain.

Transport and localization of interface. The initialization of the scalar field $F(x, y, t)$ is performed over the entire domain such that the initialization value is constant outside the initial cursor position which is between the inlet sections $x = 0$ and $0{\cdot}04$ m. Inside the initial cursor position the distribution of the field F is

$$F(x, y, t_0) = -200x + 4 \quad \text{for } 0 \leqslant x \leqslant 0{\cdot}04.$$

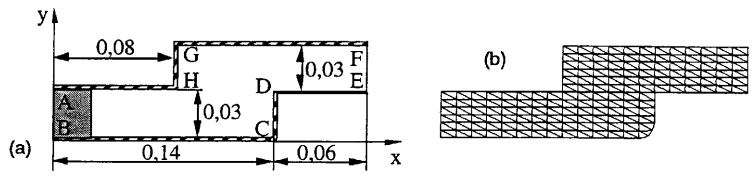

Figure 17. (a) Geometry of problem; (b) mesh of fluid flow domain

The initial position of the interface is given as $x = 0{\cdot}02$ with the corresponding index value $F_c = 0$. This index value will define the successive interface positions in the domain.

The problem of interface transport is purely convective. Consequently, we simply impose a Dirichlet boundary condition on the inlet section AB:

$$F(0, y, t) = 4 \quad \text{for } 0 \leqslant y \leqslant 0{\cdot}03.$$

The filling simulation is obtained with 200 time steps of an implicit Euler scheme. The minimum value of the time step is $\Delta t = 0{\cdot}01$ s. The successive interface positions and corresponding velocity fields during the filling process are displayed in Figure 18.

4.4. Filling of a casting mould

In this example we present a comprehensive simulation of the filling stage of a casting mould whose geometry is presented in Figure 19. It is an application of bottom-gated mould filling since the liquid metal enters at the base. Cast iron is the liquid metal introduced into the mould. It gradually displaces the air previously in the mould. The physical properties of the two fluids as well as the properties of the sand constituting the mould walls are the following.

$$\begin{array}{lll}
\rho_1 = 6700 \text{ kg m}^{-3}, & \rho_2 = 1{\cdot}1 \text{ kg m}^{-3}, & \rho_3 = 1500 \text{ kg m}^{-3} \\
\mu_1 = 15 \times 10^{-3} \text{ Pa s}, & \mu_2 = 1 \times 10^{-5} \text{ Pa s}, & \\
C_{p1} = 800 \text{ J kg}^{-1} \text{ K}^{-1}, & C_{p2} = 1005 \text{ J kg}^{-1} \text{ K}^{-1}, & C_{p3} = 1000 \text{ J kg}^{-1} \text{ K}^{-1}, \\
k_1 = 33 \text{ W m}^{-1} \text{ K}^{-1}, & k_2 = 3 \times 10^{-2} \text{ W m}^{-1} \text{ K}^{-1}, & k_3 = 1 \text{ W m}^{-1}; \text{K}^{-1}.
\end{array}$$

Physically speaking, three zones can be distinguished in the domain. Indices 1, 2 and 3 indicate respectively the liquid metal, air and sand (see Figure 19(a)). The domain is discretized by

(a) 1050 T6 elements in the mould, consisting of 2337 nodes
(b) 107 L3 elements on the inner sides of the mould
(c) 1222 T6 elements in the mould thickness (sand), consisting of 2288 nodes.

This amounts to 2380 elements and 4625 nodes (see Figure 19(b)).

We have refined the mesh on the mould sides along the shape contour which corresponds to an intense heat exchange zone between the liquid metal and the mould (Figure 20). The fluid is introduced into the mould at a temperature close to its melting temperature (about 1300 °C), while the mould is initially at ambient temperature (20 °C). This mesh refinement is necessary to accurately model the thermal gradient on both sides of the solid–liquid boundary. We thus propose a length ratio between the elements on each side of this contact, considered as perfect, assuming a pure conduction phenomenon. In this case, to express the continuity of the heat flux, the following condition must be observed:

$$\frac{a_1}{a_3}\left(\frac{l_3}{l_1}\right)^2 = 1, \quad \text{with } a_1 = \frac{k_1}{\rho_1 C_{p1}}, \quad a_3 = \frac{k_3}{\rho_3 C_{p3}},$$

where a_1 and a_3 represent the thermal diffusivities of media 1 and 3 and l_1 and l_3 are the lengths of the elements in media 1 and 3 according to the directions of the thermal gradient.

A similar refinement of the mesh should be carried out in the proximity of the interface where the same problem occurs (air is a better insulator than sand). Nevertheless, the interface displacement in time prevents this operation when there are no solution-adaptive computational grid capabilities.

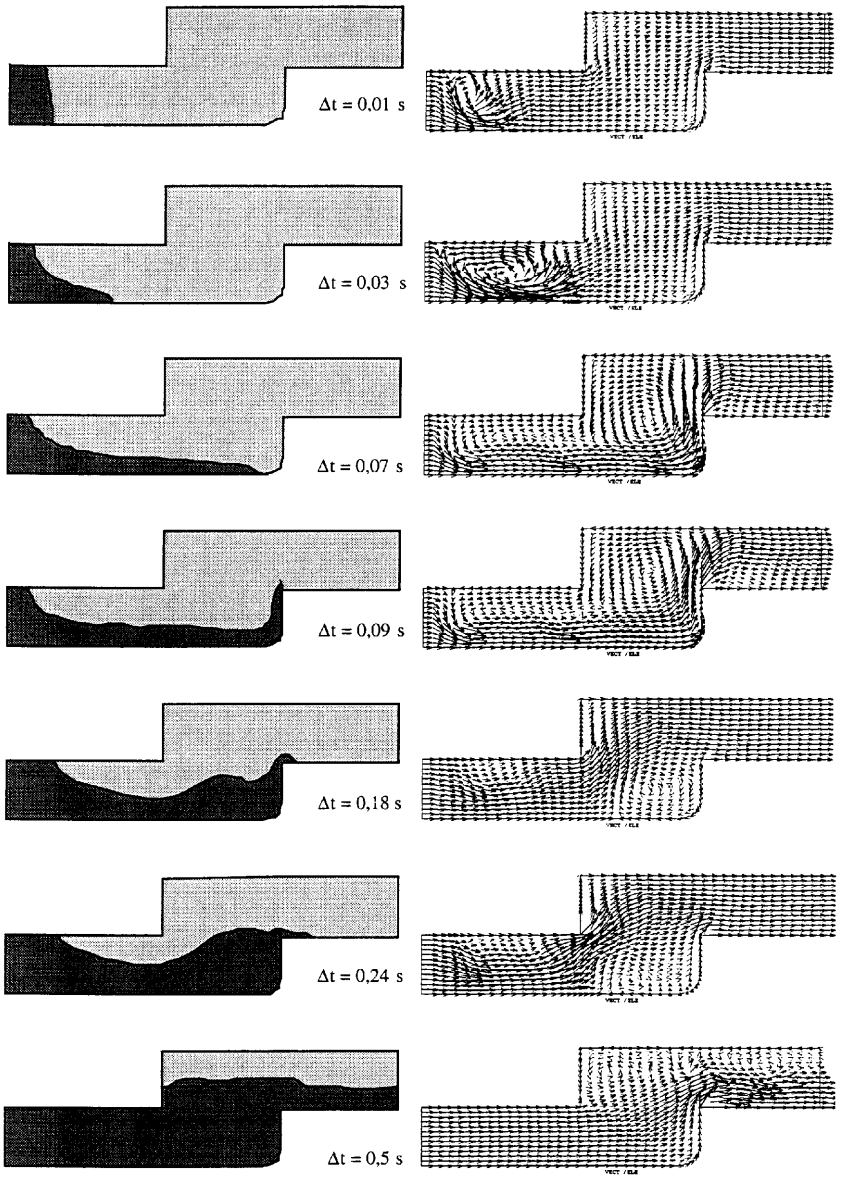

Figure 18. Interface position and corresponding velocity field

Fluid flow. The boundary conditions are expressed in the local reference frame.

1. On AB : $U_n = -0{\cdot}25$ m s^{-1} and $U_{tg} = 0$.
2. On BC and DA: $U_n = 0$ and $\tau = -\alpha U_{tg}$, with $\alpha = 0{\cdot}01$.
3. On CD: $\partial U_n / \partial n = 0$.

The initial solution is chosen to be zero over the entire domain for the flow variables.

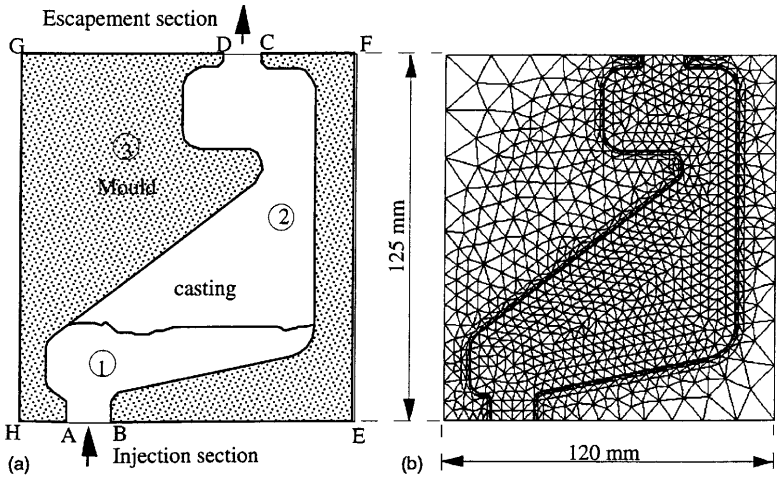

Figure 19. (a) Geometry of problem; (b) mesh of studied domain

Transport and localization of interface. Initialization of the scalar field $F(x, y, t)$ is performed over the entire domain. The initial value is set to a constant outside the initial cursor. The cursor extends from the injection section AB to the point where the neck starts bell-mouthing. Inside this initial cursor the initial distribution of the field F is

$$F(x, y, t_0) = -1000\, y + 3 \quad \text{for } 0 \leqslant y \leqslant 0{\cdot}006.$$

The initial position of the interface is given as $y = 0{\cdot}003$ with the corresponding index value $F_c = 0$. This index value will enable us to define the interface position as the mould is filled.

The interface transport problem is purely convective. That is why we only impose a Dirichlet boundary condition on the inlet section AB:

$$F(x, 0, t) = 3 \quad \text{for } 0{\cdot}015 \leqslant x \leqslant 0{\cdot}028.$$

Heat transfer. The boundary conditions are as follows:

1. On AB: $T = 1300\ ^\circ\text{C}$.
2. On HE and FG: $\partial T/\partial n = 0$.
3. On EF and GH: $T = 20\ ^\circ\text{C}$.

The initial solution of the thermal problem is constant, $T_0 = 20\ ^\circ\text{C}$, in the whole mould.

Figure 21 displays the evolution of the interface during the filling operation.

Figure 22 displays at various times the following features of the filling process:

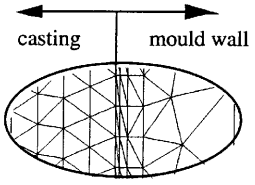

Figure 20. Refinement of mesh in mould side proximity

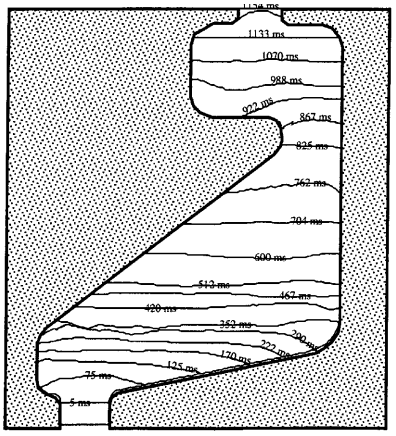

Figure 21. Superposition of some interface positions

(a) the velocity fields of the liquid cast iron and air in the mould
(b) the interface position separating the liquid cast iron which fills up the mould and air escaping (it is superposed on the velocity field in the figures)
(c) the temperature field within the flowing fluids and in the mould walls as well.

5. CONCLUSIONS

The purpose of this numerical model is the simulation of flows with complex moving interfaces. It takes advantage simultaneously of the geometrical discretization flexibility of a finite element analysis and the potential of volume-tracking methods. As a matter of fact, the approach is Eulerian and based on a fixed mesh. This avoids the problem of element distortion and therefore remeshing. Systems including complex obstacles and shapes can be represented accurately. Furthermore, the mesh can be refined locally in regions with large gradients. This possibility has been exploited in the last application presented, where very intense thermal gradients had to be taken into account near the walls.

The model efficiency is also related to the solution strategy adopted. This strategy consists of solving flow, heat transfer and interface transport problems sequentially. It allows the creation of a mesh for each problem and takes into account their own peculiarities (domain of definition, refinement zone, etc.). Furthermore, numerical schemes can be chosen individually according to the mathematical nature of the equations to be solved (hyperbolic, parabolic, non-linear, etc.).

The cursor concept has been introduced to improve the PCM front-tracking approach. It simply consists of restricting the computational domain for the front advection problem to regions where the scalar field F has non-zero gradient. In addition, a global mass conservation procedure has been implemented. It influences very slightly the front position, providing a computational grid fitted to the flow complexity.

Considering fluids on either side of the interface is also another important aspect of the model. However, this aspect is mainly an advantage for flows in confined media where both fluids can influence the interface dynamics. On the other hand, when dealing with external flows such as the dam-breaking problem, the model efficiency could be improved by simplifying the computation of the external fluid flow (pseudofluid).

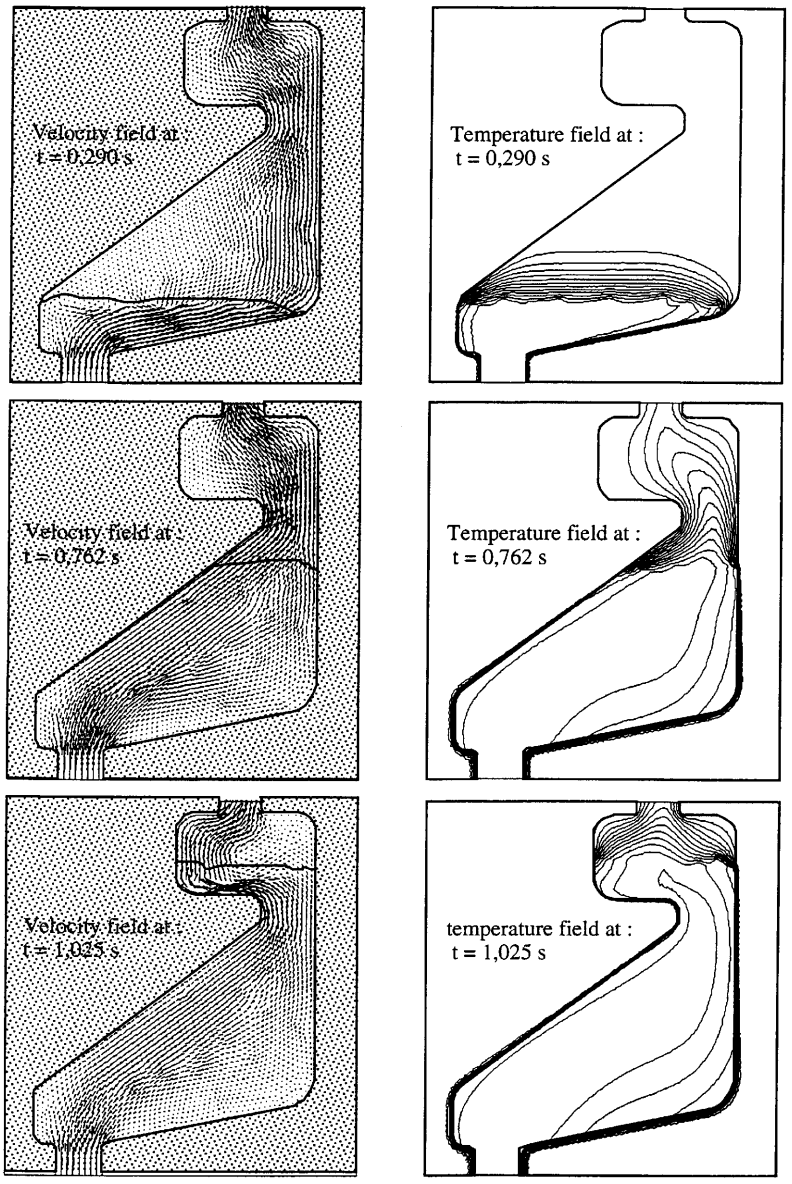

Figure 22. Interfacee positions, velocity and temperature fields

Finally, a model weakness lies in the vague representation of the interface as far as physical properties are concerned. Indeed, this difficulty is inherent in the representation of a moving interface on a fixed mesh. However, the examples presented show that this approach provides satisfactory results for situations where the methods based on a Lagrangian description of the interface are ineffective.

ACKNOWLEDGEMENT

The authors would like to thank Professor R. L. Sani for many helpful discussions.

REFERENCES

1. M. Medale, 'Modélisation numérique par la méthode des éléments finis de l'étape de remplissage des moules de fonderie', *Thèse de Doctorat*, Université de Compiegne, 1994.
2. J. M. Floryan and H. Rasmussen, 'Numerical methods for viscous flows with moving boundaries', *Appl. Meth. Rev.*, **42**, 323–341 (1989).
3. C. W. Hirt, A. A. Amsden and J. L. Cook, 'An arbitrary lagrangian–eulerian computing method for all speeds', *J. Comput. Phys.*, **14**, 227–253 (1974).
4. T. J. R. Hughes and W. K. Kiu, 'Lagrangian–Eulerian finite element formulation for incompressible viscous flow', *Comput. Methods Appl. Mech. Eng.*, **29**, 329–349 (1981).
5. B. D. Nichols and C. W. Hirt, 'Improved free surface boundary conditions for numerical incompressible flow calculations', *J. Comput. Phys.*, **8**, 434–448 (1971).
6. F. H. Harlow and J. E. Welch, 'Numerical study of large amplitude free surface motion', *Phys. Fluids*, **9**, 842–851 (1966).
7. C. W. Hirt and B. D. Nichols, 'Volume of fluid (VOF) method for the dynamics of free boundaries', *J. Comput. Phys.*, **39**, 201–225 (1981).
8. C. W. Hirt, B. D. Nichols and N. C. Romero, 'SOLA—a numerical solution algorithm for transient fluid flows', *Los Alamos Scientific Laboratory Rep. LA-5852*, 1975.
9. J. D. Ramshaw and J. A. Trapp, 'A numerical technique for low speed homogeneous two phase flow with sharp interfaces', *J. Comput. Phys.*, **21**, 438–453 (1976).
10. E. Thompson, 'Use of pseudo-concentrations to follow creeping viscous flows during transient analysis', *Int. j. numer. methods fluids*, **6**, 749–761 (1986).
11. G. Dhatt, D. M. Gao and A. Ben Cheikh, 'A finite element simulation of metal flow in moulds', *Int. j. numer. methods eng.*, **30**, 821–831 (1990).
12. R. L. Lewis, A. S. Usmani and J. T. Cross, 'Efficient mould filling simulation in castings by an explicit finite element method', *Int. j. numer Methods fluids*, **20**, 493–506 (1995).
13. C. Hirsch, *Numerical Computation of Internal and External Flows*, Vols 1 and 2, Wiley, 1990.
14. M. Jaeger, 'Simulation numérique d'écoulements turbulents incompressibles et isothermes de fluides newtoniens par éléments finis tridimensionnels', *Thèse de Doctorat*, Université de Compiègne, 1990.
15. S. V. Patankar and D. B. Spalding, 'A calculation procedure for heat, mass and momentum transfer in three dimensional parabolic flows', *Int. J. Heat Mass Transfer*, **15**, 1787–1806 (1972).
16. G. F. Carey and J. T. Oden, *Finite Elements*, Prentice-Hall, Englewood Cliffs, NJ, 1986.
17. J. V. Daurelle, R. Occelli and R. Martin, 'Finite element modelling of radiation heat transfer coupled with conduction in an adapative method', *Numer. Heat Transfer B*, **25**, (1994).
18. J. N. Reddy, 'On penalty function methods in finite elements analysis of flow problems', *Int. j. numer. methods fluids*, **2**, 151–171 (1982).
19. O. A. Ladyzhenskaya, *The Mathematical Theory of Viscous Incompressible Flows*, Gordon and Breach, New York, 1969.
20. I. Babuska and A. K. Aziz, *Survey Lectures on the Mathematical Foundations of the Finite Element Method*, Academic, New York, 1972.
21. F. Brezzi, 'On the existence, uniqueness and approximation of saddle-point problems arising from Lagrangian multipliers', *Recy. Oper. Numer. Anal.*, **R2**, 129–151 (1974).
22. M. Bercovier and O. Pironneau 'Error estimates for the finite element method solution of the Stokes problem in primitive variables', *Numer. Meth.*, **33**, 211–224 (1979).
23. J. C. Martin and W. J. Moyce, *Philos. Trans. R. Soc. Lond. A*, **244**, 312 (1955).
24. N. Brooks and J. R. Hughes, 'Streamline upwind/Petrov–Galerkin formulations for convection dominated flows with particular emphasis on the incompressible Navier–Stokes equations', *Comput. Methods Appl. Mech. Eng.*, **32**, 199–259 (1982).

